Atomistic-informed kinetic phase-field modeling of non-equilibrium crystal growth during rapid solidification

Sepideh Kavousi¹, Vladimir Ankudinov², Peter K. Galenko^{3,4}, and Mohsen Asle Zaeem^{1*}

Department of Mechanical Engineering, Colorado School of Mines, 1500 Illinois Street,
Golden, Colorado 80401, USA

ABSTRACT

A novel method based on molecular dynamics (MD) is developed to make the kinetic phase-field (PF) model quantitative in predicting non-equilibrium crystal growth during rapid solidification. MD-calculated variations of the diffuse solid-liquid (SL) interface width versus interface velocity are used to parameterize the kinetic PF model. Two approaches are adopted to study temperature independent and temperature dependent interfacial properties on the accuracy of predictions. MD simulations of slow and rapid solidification regimes for an fcc metal (Ni) show that the SL interface width decreases by increasing the solidification velocity. Fitting the dynamic response of the interface width to the traveling wave solution of hyperbolic PF equation determines the target SL interfacial properties, namely propagation velocity and diffusion coefficient. Independently, the MD calculations of nonlinearity in velocity versus undercooling is used to validate the atomisticinformed kinetic PF model. Both parabolic and kinetic PF models parameterized by temperatureindependent material properties can accurately simulate the linear portion of near-equilibrium crystal growth during solidification. However, they both fail to predict the crystal growth kinetics during rapid solidification. The kinetic PF model parameterized with the temperature-dependent SL interfacial properties can accurately predict both the equilibrium and non-equilibrium crystal growth during slow and rapid solidification. MD simulation results on Ni along with some analytical analysis on the variation of interface width versus interface velocity show that for fcc metals, in general, {110} interface has a smaller propagation velocity in comparison to {100} interface, resulting in a larger non-linear behavior at smaller undercooling.

Keywords: Rapid Solidification; Kinetic phase-field; Molecular dynamics; Non-equilibrium crystal growth.

² Theoretical Department, Vereshchagin Institute of High Pressure Physics, Russian Academy of Sciences, Moscow (Troitsk), 108840 Russia

³ Physikalisch-Astronomische Fakultät, Friedrich-Schiller-Universität Jena, 07743 Jena, Germany

⁴ Ural Federal University, Department of Theoretical and Mathematical Physics, Laboratory of Multi-Scale Mathematical Modeling, Ekaterinburg, 620000 Russia

^{*}Corresponding author: <u>zaeem@mines.edu</u> (M. Asle Zaeem)

1. INTRODUCTION

Recent technological advancements in manufacturing processes enable access to cooling rates as high as 10^6 - 10^7 (K/s) for processes such as melt spinning and laser melting [1-5]. Obtaining such a large cooling rate and the resulting large solidification velocity requires imposing a high thermodynamic driving force [6-11]. For temperatures close to the melting point, a linear correlation is held between the solidification velocity and undercooling [12]. A larger drop in temperature below the melting point decreases the mobility of atoms, which decreases the kinetics of solidification and slows down the interface velocity. Various theoretical [13-16] and computational models [17, 18] are developed to investigate non-equilibrium crystal growth.

1.1. Kinetic Growth Models

The diffusion-limited theory (DLT) [13, 14] and the collision-limited theory (CLT) [15, 16] provide a quantitative description of the solidification kinetics. Depending on the sort of particles and the conditions for their detachment/attachment from/to the solid-liquid (SL) interface, these two theories satisfactorily describe the interface velocity with a relatively small driving force, i.e., for relatively small values of overheating or undercooling of pure material. Indeed, experimental and atomistic modelling data show the existence of a good quantitative description in the narrow temperature range around the melting point where the interface velocity linearly depends on overheating/undercooling [17, 19, 20]. With the increase of the driving force, the predictions of DLT and CLT clearly contradict the data of atomistic modelling [21]. The quantitative disagreement between DLT and CLT occurs in the temperature range where the interface velocity exhibits non-linearity depending on the increased undercooling at the interface [22, 23]. The non-linearity presents a maximum at a fixed undercooling [24] and the value of maximum depends on saturation [25].

1.2. Phase-Field Models

Phase-field (PF) models based on the partial differential equations of the parabolic type (i.e., parabolic PF models) have been applied to estimate crystal growth kinetics [26-34]. These models provide quantitative predictions of microstructure evolution only at low solidification velocities and small driving forces of solidification [35-37], and they are unable to simulate high solidification velocities caused by large driving forces. Indeed, the vanishing chemical potential gradient jump at the interface, which is a basic theoretical statement of parabolic PF models, implies the instant establishment of local thermodynamic equilibrium. This instant-appeared fluxes avoid the details of local diffusional changes and microstructural reconstructions, which are principally substantial in rapid solidification where non-linearity in the crystal growth kinetics is expected. As a result, the parabolic PF models are unable to predict the behavior of the interface motion under a wide range of driving forces, specifically, the non-linearity in the velocity-undercooling relationship obtained in molecular dynamics (MD) simulation of rapid solidification [38].

Several modifications have been proposed to improve the predictions of the parabolic PF models as they are applied to investigate rapid solidification. Non-linear driving forces at large undercooling [39, 40] or temperature-dependent material properties [41] were introduced as an alternative method to address the shortcomings of parabolic PF models. However, the accuracy of these models drops in the regimes where nonlinearity governs the velocity-undercooling relationship. Bragard et al. [39] modified the driving force term in the PF free energy formulation from a linear to a power-law dependence on undercooling to manipulate the onset of velocity-undercooling deviation from linearity. However, this modification was not physics-based, and the power-law correlation depended on the 1D solution of the PF model. Attempts to describe non-linearity in the crystal growth kinetics using the parabolic PF model are limited so far to a small interval of driving forces [42] in comparison with the wide range of undercooling attained in atomistic simulations [22, 24, 43].

1.3. Rapid Solidification as a Local Non-Equilibrium Process with Violating Ergodicity

In rapid solidification, the time necessary for freezing of local volumes might have a microscopic scale comparable with the time required for establishing local thermalization and local thermodynamic equilibrium. In other words, SL interface velocity may become comparable to the rate of leveling out of the structural and/or chemical inhomogeneity in the local volume of the sample. In this case, the process of solidification is defined as the rapid solidification due to the intense attachment of the particles from liquid to solid at a large driving force [9-11]. Similarly, the high-frequency nucleation of crystals and their propagation in the volume (for instance, through the explosive mechanism) may result in fast freezing of the sample [44].

In the case of pure substances, the interface velocity should be comparable to the speed of heat propagation or to the characteristic maximum speed of the order parameter. Thus, rapid solidification is defined by the absence of time for local thermalization, i.e., local relaxation of heat, or local chemical/structural relaxation, that leads to the violation of ergodicity [11].

To achieve local equilibrium in pure substances at large driving forces, the relaxation of the gradient flow as the relaxation of the rate of change of the order parameter (φ) is used in consistency with the formalism of irreversible thermodynamics [44]. Therefore, the equation of order parameter evolution includes both the temporal change of gradient flow, (acceleration: $\partial(\partial\varphi/\partial t)/\partial t$), as well as the relaxation of order parameter (velocity: $\partial\varphi/\partial t$).

Using the PF relaxation together with the gradient flow relaxation is the key difference between the kinetic PF model and the existing parabolic ones [45, 46]. The kinetic PF model is based on the transport and interface dynamic equations as the partial differential equations of hyperbolic type. This hyperbolic dynamic gradually transforms into parabolic transport and parabolic PF dynamics by decreasing the driving force.

1.4. The Kinetic Phase-Field Model and Its Parameters

The kinetic PF model is based on the hyperbolic equations, including the first and second derivatives of the order parameter with respect to time. This model allows the process analysis to be performed at short time periods comparable with the freezing of local volumes. Thus, one can quantitatively evaluate the locally non-equilibrium states [17, 18]. These states are responsible for the nonlinearity in the interface velocity as observed in experimental studies of glass formation alloys [46] or MD simulations [17, 18, 22, 47-49].

In addition to the known capillary and kinetic parameters of the parabolic PF models, such as interface mobility and diffusion coefficients, the kinetic PF model depends on an additional parameter, namely the relaxation time for the gradient flow. Currently, this parameter is manually tuned in such a way that it provides a fit of the kinetic PF model predictions to the MD or experimental solidification velocity versus undercooling data [17, 18, 47, 48, 50]. These previous studies only showed the potential of the kinetic PF model in predicting the growth and melting of crystals. To investigate the efficiency of the kinetic PF model in simulating solidification under large driving forces, one needs to first provide a quantitative description of the kinetic model by relating the relaxation time to material properties that are obtainable from MD simulation or experiments. To the best of our knowledge, there are no reports on experimental measurement of these properties. Therefore, an *atomically informed kinetic PF model* should be developed, starting from the previous advancements of the atomically informed parabolic PF models.

MD simulations can provide SL interfacial properties that are essential for parametrizing parabolic PF models of solidification, such as anisotropic SL interface energy [51-53], growth kinetic coefficient [54, 55], and diffuse interface velocity [55, 56]. These measurements and calculations have led to the development of multi-scale computational frameworks for investigating the microstructure evolution during solidification of metals [40, 41] and alloys [57] based on parabolic PF models.

In the present study, we integrate MD simulations with a kinetic PF model to develop a computational framework for multiscale modeling of both slow and rapid solidification. We study solidification from Ni melt, and we test the kinetic PF model predictions versus MD calculations of velocity-undercooling trends. We first develop a method for obtaining the kinetic PF parameters using MD calculations of the target material properties, namely the maximum PF propagation speed and PF diffusion coefficient. Then, we use independent MD results of nonlinearity in velocity versus undercooling to test the kinetic PF model predictions. We show the high accuracy of the kinetic PF model in a wide range of solidification rates, which can open up the possibility of its application to significant practical problems and phenomena occurring in additive manufacturing, atomization, melt spinning, laser annealing, among others [51].

2. METHODOLOGY

2.1. Phase-Field Modeling

The evolution of order parameter, φ , in the kinetic PF model is described by the partial differential equation of the hyperbolic type [58]:

$$\tau_{\varphi} \frac{\partial^2 \varphi}{\partial t^2} + \frac{\partial \varphi}{\partial t} = -M_{\varphi} \left(\frac{\delta F}{\delta \varphi} \right) \tag{1}$$

where F is the free energy, M_{ϕ} is the mobility, and τ_{ϕ} is the relaxation time of the gradient flow which helps to describe the non-linear behavior of the SL interface velocity at large driving forces [17]. The first term in the left-hand side of Eq. (1) describes relaxation of the gradient flow (acceleration), and the second term gives the relaxation of the PF itself (velocity). Both relaxations proceed under the driving force proportional to $\delta F/\delta \phi$, which is given by the right-hand side of Eq. (1). With $\tau_{\phi} \rightarrow 0$, Eq. (1) transforms to the equation of Mandel'sham and Leontovich [59] which is also known as the time-dependent Ginzburg-Landau equation [60, 61] in the parabolic PF model (see Ref. [62] and references therein). From Eq. (1), in particular, it is easy to obtain an equation for the propagation of bacteria (the Fisher-Kolmogorov-Piskunov-Piotrovsky equation of diffusion with a delay [63, 64]) or an equation for describing "order-disorder" (the Allen-Cahn equation [65, 66]).

The total free energy of the system can be written in the form of Ginzburg-Landau type free energy:

$$F = \int \left[\frac{\varepsilon(\hat{n})^2}{2} |\nabla \phi|^2 + f_{dw}(\phi, T) \right] dV \tag{2}$$

$$f_{dw}(\phi, T) = w\phi^2 (1 - \phi)^2 + \phi^3 (10 - 15\phi + 6\phi^2) \frac{\Delta H_m}{T_m} (T - T_m)$$
 (3)

The first and second terms in Eq. (2) are the excess free energy due to the interface and bulk free energy density (f_{dw}) , respectively. w is the height of the double well, ΔH_m is the enthalpy of fusion, and T_m is the melting point. Quantitative investigations of the kinetic process at the SL interface require an accurate estimation of the PF parameters for Eq. (1), namely M_{ϕ} and τ_{ϕ} , based on the SL material properties. Similar to the thin interface analysis of Ref. [62], M_{ϕ} is correlated to the anisotropic kinetic coefficient and the SL interface free energy [40]. Using MD technique for study of nickel (Ni) crystal growth, determination of capillary and kinetic properties of the diffuse interface between liquid and solid phases facilitates obtaining M_{ϕ} .

The hyperbolic Eq. (1) has the one-dimensional traveling-wave solution in the steady-state regime of the interface motion with the constant velocity, V [67]. The solution is described by the hyperbolic tangent function of the following form: $\varphi(x - Vt) = 0.5[1 - \tanh(x - Vt)/\ell]$, which is obtained under the following boundary conditions: $\varphi \to 1$ as the moving coordinate is $x - Vt \to -\infty$ (crystal) and $\varphi \to 0$ at $x - Vt \to +\infty$ (liquid). The crystal growth velocity V

(solidification regime) in this solution is given by:

$$V = \frac{\mu (\Delta T) \Delta T}{\sqrt{1 + (\mu (\Delta T) \Delta T / V_{\varphi}(\Delta T))^{2}}}$$
(4)

The kinetic coefficient of growth μ , the maximum PF propagation speed V_{φ} , and PF diffusion coefficient D_{φ} in Eq. (4) are strong functions of the kinetic undercooling ΔT at the interface, and only τ_{φ} is taken independent of temperature, which are given by

$$\mu \left(\Delta T \right) = \frac{\Delta H_m}{\gamma T_m} D_{\varphi} (\Delta T) \tag{5}$$

$$V_{\varphi}(\Delta T) = \left(D_{\varphi}(\Delta T)/\tau_{\varphi}\right)^{1/2} \tag{6}$$

$$D_{\varphi}(\Delta T) = D_{\varphi}^{0} exp\left(-\frac{E_{A}/k_{B}}{T_{m} - \Delta T}\right) \tag{7}$$

where D_{φ}^{0} is the diffusion pre-factor, E_{A} is the energetic barrier, and k_{B} is the Boltzmann constant.

The sharp-interface limit of the hyperbolic Eq. (1) has the form of an acceleration-velocity Gibbs-Thomson-type equation for the isotropic interface and an acceleration-velocity-Herring-type equation for the anisotropic interface, see Ref. [68] and references therein. These two cases also define the second equation for the velocity dependent interface width, given by the following equation.

$$\ell = \begin{cases} l_0, & if \ V = 0 \\ l_0 \left[1 - \frac{V^2}{V_{\varphi}^2} \right]^{1/2}, & if \ V < V_{\varphi} \\ \to 0, & if \ V \to V_{\varphi} \end{cases}$$
 (8)

As Eq. (8) shows, the diffuse interface width ℓ takes a constant value of l_0 in static equilibrium V=0 which is always different from its corresponding value when $V\neq 0$. ℓ tends to zero with the transition to sharp interface as soon as the interface velocity approaches the maximum speed V_{φ} for the PF propagation. Such variety in ℓ allows us to quantitatively estimate the interface width in dynamics at low and high interface velocities. Therefore, one of the methods to determine the relaxation time τ_{φ} or the speed V_{φ} is related to the determination of the diffuse interface width ℓ as a function of the crystal growth velocity V and equilibrium mean interface width ℓ_0 .

2.2. Simulation of Solid-Liquid Co-existence by Molecular Dynamics

In our present study, MD simulations are used as a tool to determine the change of interface width ℓ with the interface velocity V and to calculate the maximum PF propagation speed V_{φ} and relaxation time τ_{φ} of the gradient flow. We perform MD simulations using the non-equilibrium free solidification method [69], where the driving force of solidification is applied to the system, and the behavior of the SL interface under the applied driving force is investigated. With this aim,

all the simulations start with the coexistence of solid and liquid at the melting point. In this study, the interatomic potential developed by Kavousi et al. [70] is used for the MD simulations. This potential is based on the second nearest-neighbor modified embedded-atom method formalism and accurately predicts the low temperature properties (e.g., elastic constants, defect formation energy, surface energy, etc.) and high temperature properties (e.g., melting temperature, enthalpy of melting, etc.) of Ni.

As shown in Figure 1(a), the orthogonal directions parallel to the x-axis and y axis are chosen lateral to the solidification front, and the third direction parallel to the z-axis is chosen along with the SL interface normal direction. For $\{100\}$ crystallographic face, the simulation system is initialized with a face-centered cubic (fcc) lattice including $10\times10\times120$ unit-cells (48000 atoms), where the system is elongated in the z-direction. The effect of interface curvature is eliminated by considering small dimensions in the x and y directions. In order to determine a proper size of the simulation system, we investigated the temperature fluctuations during the NPT equilibration process at the melting point. A standard deviation smaller than 1 K for the temperature during the equilibration process was considered as the desired accuracy. Therefore, we kept the number of thermostats constant and changed the system size from $5\times5\times60$ to $20\times20\times180$ unit-cells. The standard deviation for temperature variations that we obtained during the equilibration process for the system with $10\times10\times120$ unit-cells was 0.80, which met our accuracy criterion.

The simulation system is equilibrated for 100 ps under a constant Number-Pressure-Temperature (NPT) ensemble, with the zero pressure, P = 0, and the temperature is set to the melting point (1726 K for this interatomic potential [70]). Then, the central three-fourth of the simulation system, as presented in Figure 1(a), is melted by heating the system up to 3000 K, under a constant Number-Volume-Temperature (NVT) ensemble for 40 ps, while the rest of the system remains in the original (solid) state. Then the temperature of the whole system is scaled down to the melting point, and the system is equilibrated under NPzzT ensemble for 200 ps. In this ensemble, only the normal stress in the z-direction is set to be zero, and the simulation box size can be modified in this direction only. This generates a system with SL coexistence at the melting temperature, and it is used as the initial configuration for further simulations of the solidification process.

The variation of SL interface velocity with applied undercooling is used to perform non-equilibrium free solidification simulations. The applied undercooling ranges between 25 K and 400 K. Performing the solidification simulations requires to have the lattice parameter of the solid phase at the undercooled temperature. This is obtained by separate MD simulations on a system with 4000 atoms (10×10×10 unit-cells) which is equilibrated for 80 ps at the undercooled temperature with an NPT ensemble, followed by an additional 80 ps simulation during which the mean lattice parameter is determined.

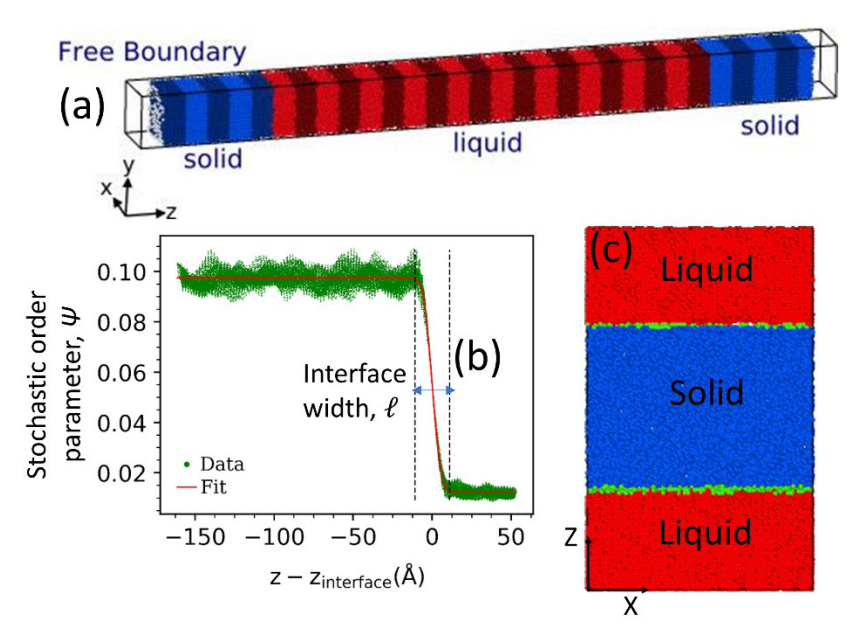


Figure 1. a) Initial configuration of the MD simulation system for the dynamic interface width ℓ calculations. The blue and red colors indicate the solid and liquid phases, respectively. The dark/light shades demonstrate the slabs that are thermostatted separately. b) The order parameter (ψ) versus the distance from the interface. The positive and negative signs of distance from interface correspond to the liquid and solid phases, respectively c) A snapshot of the simulation system used for calculations of SL interface energy. Atoms located at the SL interface are colored green.

Starting from the SL coexistence configuration, the temperature of the simulation system is scaled down to the target temperature, and the solidification is performed under the NP_{zz}T ensemble. Previous studies showed that by using just one global thermostat in the MD simulation, the temperature in the region close to the SL interface becomes larger than the rest of the system due to the release of latent heat [40, 54]. This problem is resolved by replacing the global thermostat in the simulation with multiple local ones [54]. The domain is divided into a set of regions along the z direction and each region is thermostated independently. The simulation box in the x and y directions is adjusted such that the solid region has the appropriate lattice parameter at the target temperature. The simulations are repeated for {110} and {111} SL crystallographic faces (including $7 \times 10 \times 84$ and $8 \times 7 \times 70$ unit-cells, respectively) with approximately similar numbers of atoms as the {100} crystallographic face.

Calculations of maximum PF propagation speed V_{φ} and relaxation time τ_{φ} of the gradient flow require determination of the interface velocity V and the diffuse interface width ℓ at different values of undercooling. Therefore, one should first accurately identify the interface position using a local order parameter. The order parameter used in this study was introduced by Sun et al. [71], where for each atom, the positions of its neighbors are compared with the perfect crystal. For the

 j^{th} atom, the order parameter, β_j , is calculated from the difference between the position vectors of its N neighbors and the same vectors in a perfect crystal, $\overrightarrow{r_{pc}}$, and is given by:

$$\beta_j = \frac{1}{N} \sum_{i} \left| \overrightarrow{r_i} - \overrightarrow{r_{pc}} \right|^2 \tag{9}$$

For Ni with an fcc crystal structure, first and second nearest neighbors are considered in the order parameter calculations (N=14). The order parameter calculated by this method exhibits large fluctuations. A smoothing procedure is then employed based on the method developed by Asadi et al. [72, 73]:

$$\psi(x, y, z) = \frac{\sum_{i} w_d r_i \beta_i}{\sum_{i} w_d r_i}$$
 (10)

where $w_d = [1 - (r_i/d)^2]^2$, $r_i = \sqrt{(x_i - x)^2 + (z_i - z)^2}$, and d is a smoothing distance equal 2.5a, and a is the lattice parameter at the target temperature. The xy cross-section of the simulation system is divided into grids with a spacing of 0.5a. For each grid, the position of the interface and interface width are estimated from the error function fitting to ψ as a function of distance from the interface, $z - z_{int}$:

$$\psi = \frac{1}{2} \left(\left(\langle \psi_{sol} \rangle + \langle \psi_{liq} \rangle \right) - \left(\langle \psi_{sol} \rangle - \langle \psi_{liq} \rangle \right) erf \left[\frac{z - z_{int}}{\sigma \sqrt{2}} \right] \right)$$
 (11)

where $\langle \psi_{sol} \rangle$ and $\langle \psi_{liq} \rangle$ are the average order parameters in the bulk solid and liquid phases, respectively. Although $\langle \psi_{sol} \rangle$ and $\langle \psi_{liq} \rangle$ can be obtained from separate bulk solid and liquid simulations, we consider them to be adjustable parameters along with σ and z_{int} . σ scales the width of the error function, and z_{int} determines its center. The interface width can be defined as the region where the error function ranges between $\langle \psi_{sol} \rangle$ and $\langle \psi_{liq} \rangle$, as presented in Figure 1(b). The position of the interface is taken by ψ as a halfway between $\langle \psi_{sol} \rangle$ and $\langle \psi_{liq} \rangle$ values. For each frame, the mean position of the interface and interface width is estimated by averaging the corresponding values for all the grids. The basic idea of introducing an order parameter to identify the SL interface in MD simulations is analogous to PF modeling. However, the values of the order parameter in each phase and the interface width values are not similar.

Anisotropic SL interface free energy is another material property that is essential in estimating both M_{φ} and τ_{φ} . In this study, we use the capillary fluctuation method (CFM), where the interface stiffness is calculated through the fluctuations of the SL interface [51]. Figure 1(c) is a snapshot of the simulation system where solid and liquid phases are in full equilibrium. The SL interface is a quasi-2D interface, the interface width W along the x-direction is much longer than its thickness b along the y-direction, Figure 1(c), and the interface fluctuations are investigated along the x-direction. Consider h(x) is the position of the interface along the x direction. The deviation from the average position of interface, $\langle h \rangle$, can be re-written as the summation of Fourier modes: $h(x) - \langle h \rangle = \sum_k A(k) e^{ikx}$, where A(k) is the Fourier amplitude and k is the wave number of Fourier modes. In CFM, the stiffness of interface, $y + d^2 y/d \theta^2$, is calculated using [51]:

$$\gamma + d^2 \gamma / d\theta^2 = \frac{k_B T}{bW\langle |A(k)|^2 \rangle k^2}$$
 (12)

 γ is the interface free energy, and θ is the angle between instantaneous local interface normal and the average orientation of the face. The slope of Fourier amplitudes versus the reciprocal of Fourier modes denoted the stiffness.

The interface free energy is an anisotropic property depending on the SL crystallographic face. The relation between the interface free energy and interface normal, \hat{n} , is represented as [74]:

$$\gamma(\hat{n}) = \gamma_0 \left[1 + \delta_1 \left(Q - \frac{3}{5} \right) + \delta_2 \left(3 Q + 66S - \frac{17}{7} \right) + \delta_3 \left(5Q^2 - 16S - \frac{94}{13}Q + \frac{33}{13} \right) \right]$$

$$Q = n_1^4 + n_2^4 + n_3^4, \ S = n_1^2 n_2^2 n_3^2$$

$$\tag{14}$$

where n_i (i = 1,2,3) are the components of \hat{n} in x-, y- and z-directions, γ_0 is the mean SL interface free energy, δ_j (j=1,2,3) are the anisotropy parameters, respectively [51]. The mean interface free energy and anisotropy parameters are calculated by performing MD simulations for multiple crystallographic faces, calculating the stiffness and comparing it to the corresponding expression based on Eq. (13) [40].

For an [001] crystallographic face, we used a system with 50×4×80 fcc unit cells (6400 atoms) with the [001] face along the z-direction. For the {110} crystallographic face, the number of unit cells along each spatial direction is modified such that the computational domain is of a similar size. Similar to the non-equilibrium free solidification simulations, interface energy calculations require a fully equilibrated SL coexistence. The details for SL equilibration are analogous to the one discussed previously except for the equilibration time, which is set to 1 ns in this set of simulations. After completing the equilibration process, the NPH ensemble is performed for 240 ps. During this step, the system configuration is saved every 1 ps for further analysis of the interface fluctuations. The order parameters given by Eqs. (9)-(11) are used to find the interface position. All the MD simulations are performed by the Large-scale Atomic/Molecular Massively Parallel Simulator (LAMMPS) software [75]. The post-processing of MD simulations is carried out using python packages and libraries such as MDTraj [76] and lmfit [77]. We used Ovito [78] for visualizing the trajectory files.

3. RESULTS AND DISCUSSIONS

Several independent solidification simulations have been performed utilizing the same SL coexistence at the melting point as the initial condition. Random seed numbers were chosen in thermostat settings to replicate independent MD simulations through a different initial velocity distribution in the system. Each of the system replicas has a fixed overall temperature of all the atoms, but a different set of velocities for atoms on each processor. This ensures, for each undercooling, each simulation is independent. To determine the uncertainties of simulated data, simulations with undercoolings up to 100 K were repeated four times, and simulations with larger undercoolings, corresponding to larger interface velocities, were repeated eight times.

3.1. Growth Kinetics

Figure 2 summarizes the interface velocity—undercooling relationship for the three investigated faces. For small values of undercooling, the interface velocity for all three faces follows a linear relationship characterized by the kinetic coefficient μ as the slope [25]. The kinetic coefficient is the first material property calculated by MD [62] that is used in parameterizing the kinetic PF model. As the undercooling increases, the interface velocity gradually deviates from the linear behavior. The curves in Figure 2 show that the non-linearity of the velocity is represented by the curves with saturation, i.e., curves have a clear tendency to reach maximum value asymptotically, as in the previous work of Hoyt et al. [25]. In addition, there is a clear difference between the solidification nanostructure obtained by the solidification of each crystallographic face. The rate of interface velocity change versus undercooling is higher for the {100} crystallographic face, and it decreases as the crystallographic face changes from {100} to {110} and {111}. The kinetic coefficients for {100}, {110}, and {111} faces, calculated by fitting MD data to $\mu = V/\Delta T$, are 0.420, 0.277, and 0.175 m/s/K, respectively.

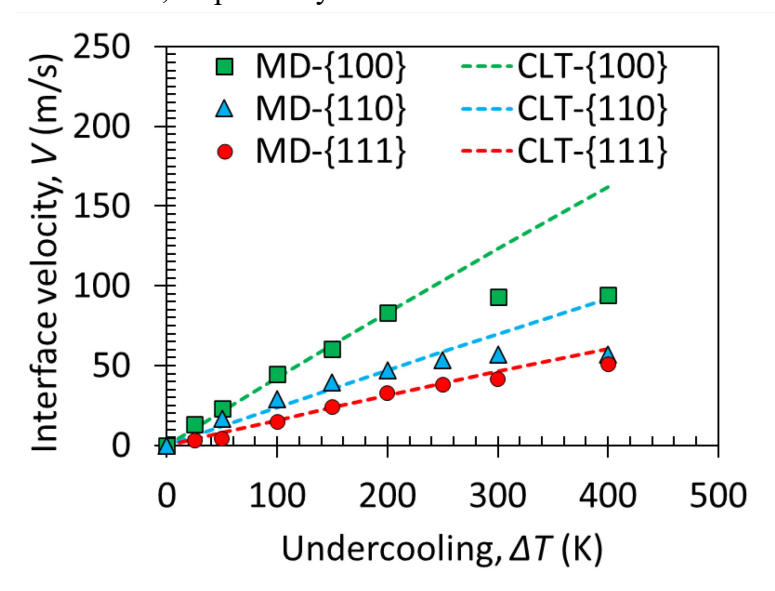


Figure 2. The interface velocity, V, versus the undercooling, ΔT , for solidification of Ni based on MD results and their fit to the CLT model. Undercooling is considered as the driving force necessary for attachment of atoms to the interface that is usually called as kinetic undercooling.

On the other hand, the CLT model provides an analytical description of the correlation between velocity and temperature as follows [16]:

$$V = C_0 \sqrt{\frac{3k_B T}{M}} \left[1 - exp\left(-\frac{\Delta G}{k_B T}\right) \right]$$
 (15)

M is the molar mass, and ΔG is the free energy change during the solidification, which can be estimated as:

$$\Delta G \approx \frac{\Delta H_m}{T_m} (T_m - T) \tag{16}$$

Fitting of the linear part of MD results to the CLT model is presented by the dotted lines in Figure 2. For {100}, {110} and {111} orientations, the maximum deviations of 71.2%, 61.1% and 18.6% are observed between the MD and CLT results at 400 K undercooling, respectively. The results clearly indicate the deviation of MD results from the CLT model as the undercooling increases, suggesting the failure of CLT model in predicting the kinetics of solidification at large undercoolings, especially for {100} and {110} interfaces. The fitting parameter (C_0) in Eq. (15) for the {100}, {110}, and {111} interfaces are 0.70, 0.40, and 0.26, respectively. Based on the CLT model [16], C_0 depends on the interplanar spacing along the target orientation. Our estimations of the ratio for kinetic coefficients $\mu_{\{100\}}/\mu_{\{110\}} \approx 1.54$ is close to $\sqrt{2}$ (≈ 1.41) predicted by CLT [16], which states that the interface velocity is proportional to the interplanar spacing. Therefore, one may say, for small undercooling, the growth of {100} and {110} faces proceeds by the collision-limited mechanism.

3.2. Anomaly in the Growth of HCP Islands during Solidification of {111} Interface

When investigating growth of the {111} crystallographic face, the ratio of kinetic coefficients is $\mu_{\{100\}}/\mu_{\{111\}} \approx 2.4$ which is much higher than $\sqrt{3}$ predicted by CLT [16]. This suggests the growth of {111} face is definitely not collision limited. The velocities calculated from MD simulations of {111} face are smaller than the CLT model predictions, which is typical for most fcc alloys [69, 71, 79, 80]. Low stacking fault energy for fcc metal is one reason for the formation of hexagonal close packed (hcp) islands in the solidified region. During the growth of the solid phase, an atom in the liquid phase can attach to sites belonging to either the fcc or hcp lattice. When the stacking fault energies are low or the driving force (undercooling) is high, hcp islands form in the solid phase [79]. Figure 3 (c) illustrates a snapshot of MD simulation during the solidification of $\{111\}$ face at $\Delta T=100$ K, where the clusters with stacking faults (hcp, red color) are formed inside the fcc phase (colored green). Both the stable and unstable generalized stacking fault energies calculated for this interatomic potential [52] are around 150 mJ/m², which is low enough for the formation of both hcp and fcc structures. The stacking fault calculations are performed by shearing a perfect crystal along a (1 1 1) plane in the $<11\overline{2}>$ direction. Details on methodology for calculating the stacking fault energy can be found in [81]. In addition, Figure 3(b) presents a snapshot of MD simulation during the solidification of {110} crystallographic face with a higher undercooling of $\Delta T = 400$ K. This suggests that large undercoolings can also lead to hep formation during the solidification of interfaces with faces other than {111}. For the {100} face in the range of undercooling ΔT <450 K, we did not observe formation of any HCP islands (Figure 3 (a)). As discussed in the methodology section, the interface velocity and position are identified using the order parameter ψ , where the position of the neighbors is compared with the perfect crystal (fcc for Ni). Thus, for the simulations that coincide with the formation of hcp

islands, calculations of interface velocity are only possible using the energy method [40], where the volumetric enthalpy change is used to determine the rate of solid phase formation and solidification velocity. Further simulations and analysis on the evolution of stress field during the formation of hcp clusters are needed to investigate how the residual stress may alter the mechanical response of the material.

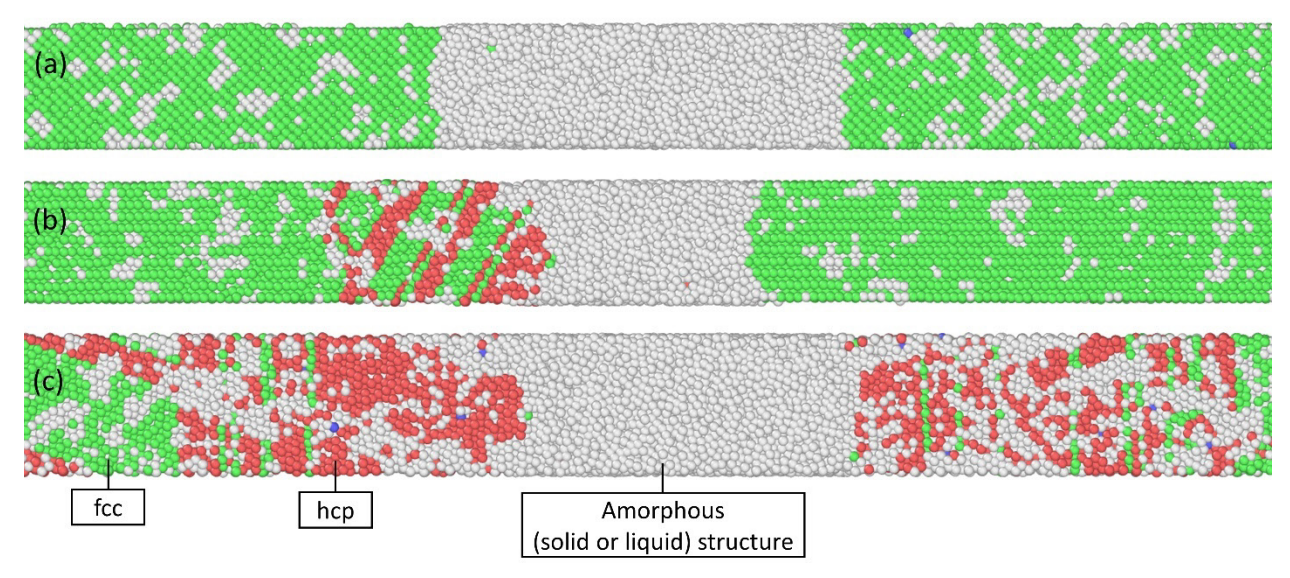


Figure 3. Snapshots of MD simulation for solidification of Ni: a) for {100} oriented crystal-melt interface and 425K undercooling, b) for {110} oriented crystal-melt interface and 400K undercooling, and c) for {111} oriented crystal-melt interface and 100K undercooling. The coloring is based on the common neighbor analysis: green atoms have FCC, red atoms have HCP and grey atoms have amorphous (solid or liquid) structure.

3.3. Stiffness and Free Energy of the Solid-Liquid Interface

The second material property that is necessary to parameterize the PF model is the anisotropic SL interface free energy. Table 1 summarizes the faces considered along x- and z-directions in the MD simulations, which are presented by crystallographic direction <...> and crystal face {...}, and the corresponding interface energy and stiffness expressions are determined by Eq. (13). As presented in Figure 4, stiffness is estimated by the slope of line fitting $k_BT/(bW\langle|A(k)|^2\rangle)$ versus k^2 for each crystallographic face. As observed in our previous studies [40, 70], the (100) oriented crystal-melt interface has the lowest stiffness (Table 1) and highest interface energy (Table 2) in comparison to the (110) and (111) oriented interfaces. This is also supported by the experimentally [82] and computationally [41] observed dendritic morphology and preferred growth direction for fcc materials. Then the MD-calculated stiffness values are fitted to the corresponding expressions to obtain the mean interface energy and anisotropy parameters. The fitting process results in γ_0 =382.1 mJ/m², δ_1 =0.0204, δ_2 =-0.00025, and δ_3 =0.0074. Results of the current MD simulation are in good agreement with the previous results using the EAM potential [83] and experiments [84].

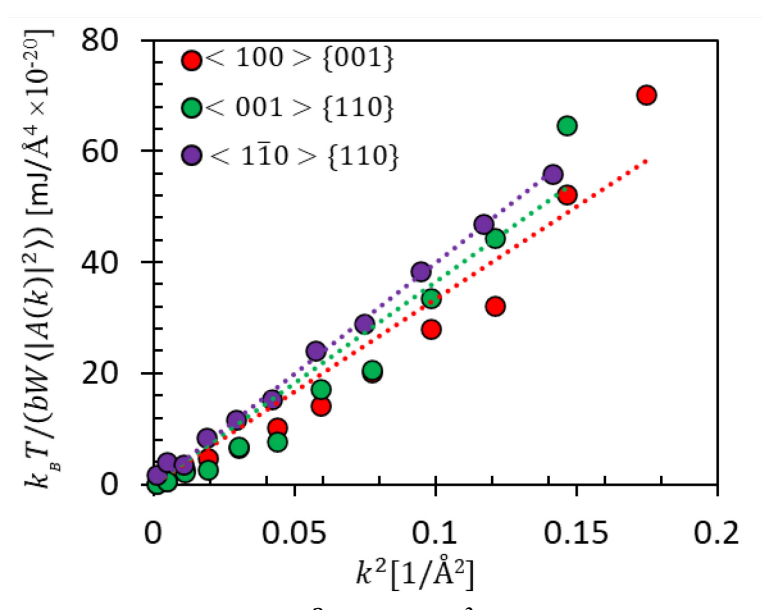


Figure 4. The variation of $k_BT/(bW\langle|A(k)|^2\rangle)$ versus k^2 for different faces as obtained from MD simulation of Ni. The dotted lines are linear fits where the color of the line is the same as the symbols for the data it was fit to Eq. (12).

Table 1. SL interface free energy and stiffness expressions for various faces as given by Eq. (13)

faces	Interface energy expression using Eq. (13)	Interface stiffness expression using Eq. (13)	Interface Stiffness - MD (mJ/m²)
(100) (001)	$\gamma_0 [1+0.4 \ \delta_1+0.571 \ \delta_2+4.31 \ \delta_3]$	$\gamma_0 [1 - 3.6 \; \delta_1 - 11.43 \; \delta_2 - 6.77 \; \delta_3]$	336
(001) {110}	$\gamma_0[1\text{-}0.1\;\delta_1\text{-}0.9286\;\delta_2\text{+}4.17\;\delta_3]$	$\gamma_0 [1 + \! 3.9 \delta_1 + 11.07 \delta_2 - 4.75 \delta_3]$	398
$\langle 1\overline{1}0\rangle \{110\}$	$\gamma_0[1\text{-}0.1\;\delta_1\text{-}0.9286\;\delta_2\text{+}4.17\;\delta_3]$	$\gamma_0 [1 \text{-}2.1 \delta_1 + 26.07 \delta_2 \text{+}0.635 \delta_3]$	365
$\langle 1\overline{1}0\rangle \{111\}$	$\gamma_0 [1\text{-}0.267 \; \delta_1\text{-}3.87 \; \delta_2\text{+}4.13 \; \delta_3]$	$\gamma_0 [1 + \! 1.2 \delta_1 + 2.97 \delta_2 + \! 12.667 \delta_3]$	408

Table 2 summarizes the material properties that are essential to parameterize both the parabolic and hyperbolic (kinetic) PF models. As discussed previously, the kinetic PF model parameterization requires additional material properties, namely maximum PF propagation speed V_{φ} and PF diffusion coefficient D_{φ} . Section 3.4 provides details of the MD simulations to calculate the aforementioned properties.

Table 2. The material properties for Ni obtained from MD simulations compared other studies [17, 39]. These material properties are used to parameterize both parabolic and kinetic (hyperbolic) PF models.

Property	This study		Literature	
Kinetic growth coefficient, μ (m/s/K)	{100}	0.420±0.015	{100}	0.52 [39]
Kinetic growth coefficient, μ (m/s/K)	{110}	0.277 ± 0.02	{110}	0.4 [39]

Interface energy, γ (J/m²)	{100} 0.397 {110} 0.393	0.326 [39]
Melting enthalpy, ΔH_m (×10 ⁹ J/m ³)	2.319	2.66 [17]
Melting temperature, T_m (K)	1728	1706 [17]

3.4. Molecular Dynamics Calculations of Material Properties Specific to the Kinetic PF Model

Performing quantitative simulations of the kinetic PF model requires accurate calculations of two other material properties, namely the maximum PF propagation speed V_{φ} and PF diffusion coefficient D_{φ} . The lack of an experimental or computational technique to calculate these material properties forces all the studies in the literature to manually modify these material properties such that the kinetic PF model predictions fit the MD or experimental solidification velocity versus undercooling data [17, 18, 47, 48, 50]. In this study, we proposed a new approach to calculate these material properties based on the traveling wave solution of the hyperbolic PF model and use them to parameterize the kinetic PF model. Details on the methodology for calculating the aforementioned material properties have already been discusses in section 2.1.

Figure 5 demonstrates the change of interface width with the solidification velocity during the growth of {100} and {110} interfaces. As discussed previously, during solidification of {111} face (for all the investigated undercoolings) and {110} face (for large undercoolings), the solid phase is a combination of HCP and FCC structures. Thus, calculations of interface width for these cases would not be accurate and are not considered in this study. In Figure 5, the green circles are the data from simulations, and the red circles are the average interface width and velocities for all the replica simulations of each undercooling. Data on variations in the average interface width (Å) and the average solidification velocity V (m/s) versus undercooling ΔT (K) for {100} and {110} SL interfaces are provided in Table A1 in the Appendix. Despite the fluctuations in the MD simulation data, the trend of the general behavior of the interface width begins to shrink as the solidification velocity increases, which is predicted by the traveling wave solution of the hyperbolic PF model and is presented by Eq. (8). The atomic spacing for an element with a perfect fcc structure is a and $a\sqrt{2}/2$ along {100} and {110} orientations, respectively. Therefore, it is expected to obtain a smaller diffuse interface width for {110} orientation. For the parabolic PF model, $au_{\phi}=0$ and the interface width would stay constant as interface velocity increases, which is not consistent with MD simulation results. As discussed in the methodology, we will take two different approaches to determine the maximum PF propagation speed and the PF diffusion coefficient, which are discussed below.

Method I: Temperature-independent material properties

In this method, the material properties used in parameterizing the PF equations are considered to be independent of temperature. Therefore, Eq. (6) reduced to:

$$V_{\varphi}^{I} = \left(D_{\varphi}^{I}/\tau_{\varphi}\right)^{1/2} \tag{17}$$

The dashed lines in Figure 5 are the fit of the MD results to Eqs. (8) and (17), and the maximum PF propagation speeds V_{φ} for {100} and {110} faces are calculated as 550±39 and 224±8 m/s, respectively. Later, the diffusion coefficient in Eq. (5) is also reduced to a constant number. D_{φ}^{I} is obtained from the reduced form of Eq. (5) [64]:

$$\mu = \frac{D_{\varphi}^{I} \Delta H_{m}}{\gamma T_{m}} \tag{18}$$

Finally, the target model parameter (τ_{φ}^{I}) is obtained by plugging in V_{φ}^{I} , D_{φ}^{I} in Eq. (17). Table 3 summarize all the material properties $(V_{\varphi}^{I}, D_{\varphi}^{I})$ and model parameters (τ_{φ}^{I}) specific to the kinetic PF model-method I. Table 3 also compares the material properties obtained by MD simulations in the current study with the ones used in kinetic PF modeling of Ni by Salhoumi and Galenko [17]. The way that these material properties are chosen in [16] is simply based on fitting the nonlinear region of interface velocity-undercooling correlation predicted by kinetic PF modeling to the MD results by Mendelev et al. [20]. This study [17] and other similar ones in the literature [18, 47, 48, 50] only highlight the potential of kinetic PF model in capturing the nonlinearity during rapid solidification. However, the potential of the kinetic PF model is not fully flourished unless we turn it into a predictive model. A predictive kinetic PF model in stead of being an input in parameterizing the model. In Section 3.5, we will investigate the accuracy of the atomistic-informed predictive kinetic PF model.

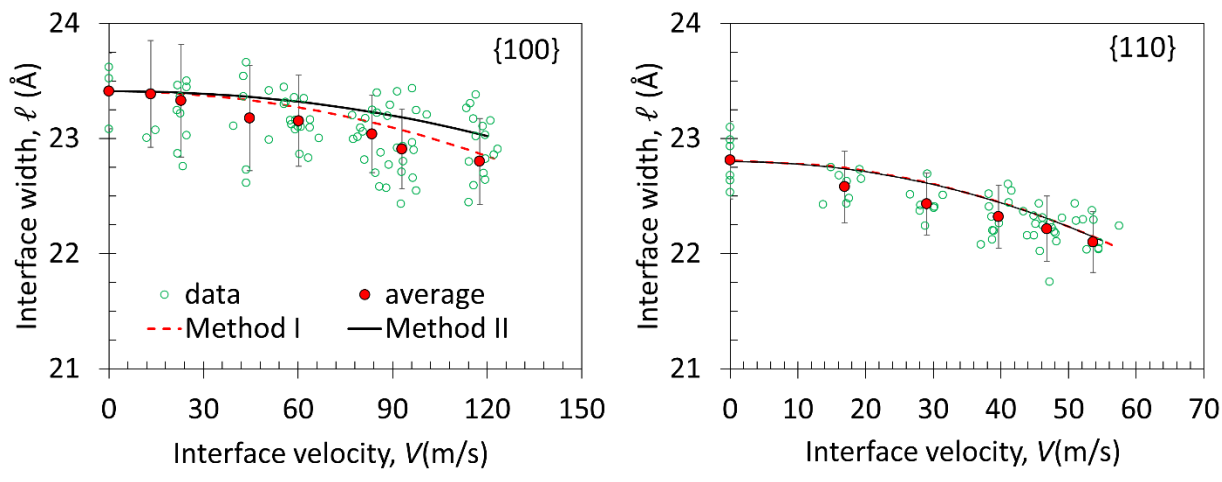


Figure 5. The change of interface width versus the solidification velocity for {100} and {110} faces. The green circles are the data for individual MD simulations, and the red circles are the average of the interface widths calculated for each undercooling. The red dashed and black solid lines are the fit of data to Method I and Method II, respectively.

Table 3. The comparison of material properties and model parameters specific to kinetic modelmethod I (temperature independent) from this study and literature [17, 39].

Property	This study	Literature	
Maximum speed of the PF, V_{φ}^{I} (m/s)	{100} 550±39	185 [17]	
with the speed of the TT , V_{φ} (111/8)	{110} 224±8	105 [17]	
PF diffusion coefficient, D_{ω}^{I} (×10 ⁻⁷ m ² /s)	{100} 1.242	1.15 [17]	
Tr diffusion coefficient, D_{φ} (\$10 m/s)	{110} 0.811	1.13 [17]	
Equilibrium diffuse interface width 1 (Å)	{100} 23.41±0.203		
Equilibrium diffuse interface width, l_0 (Å)	{110} 22.81±0.205	-	
Relaxation time of the PF gradient, τ_{φ}^{I} (s)	4.1×10 ⁻¹³	1.62×10 ⁻¹² [17]	

Method II: Temperature-dependent material properties

In this method, the material properties used in parameterizing the PF equations are temperature dependent. We use the interface width obtained from MD-data to calculate the temperature-dependent maximum speed of the PF and the PF diffusion coefficient. Indeed, $V_{\varphi}^{II}(T)$ and $D_{\varphi}^{II}(T)$ are calculated by fitting the data in Figure 5 to Eq. (8). The results are presented as functions of undercooling ΔT for {100}- and {110}-faces in Figure 6. This Figure also compares the maximum speed of the PF and the PF diffusion coefficient obtained from both methods I and II. The results suggest that the constant mean values for V_{φ}^{I} and D_{φ}^{I} obtained based on Method I (Table 3) are well quantitatively included within temperature dependent V_{φ}^{II} and D_{φ}^{II} obtained from method II. The parameters in Eq. (7) which describe the temperature-dependence behavior of $D_{\varphi}^{II}(T)$, known as D_{φ}^{0} and E_{A}/k_{B} , and the resultant model parameter for method II (τ_{φ}^{II}) are summarized in Table 4.

Table 4. The material properties and model parameter specific to the kinetic PF model (Method II) for the crystal growth of Ni.

Parameter	{100}-face	{110}-face
PF diffusion pre-factor, D_{φ}^{0} (×10 ⁻⁶ m ² /s)	0.57	0.374
Energetic barrier for PF diffusion, E_A/k_B (K)	2385	2480
Relaxation time of the PF gradient, τ_{φ}^{II} (s)	2.94×10 ⁻¹³	1.54×10 ⁻¹²

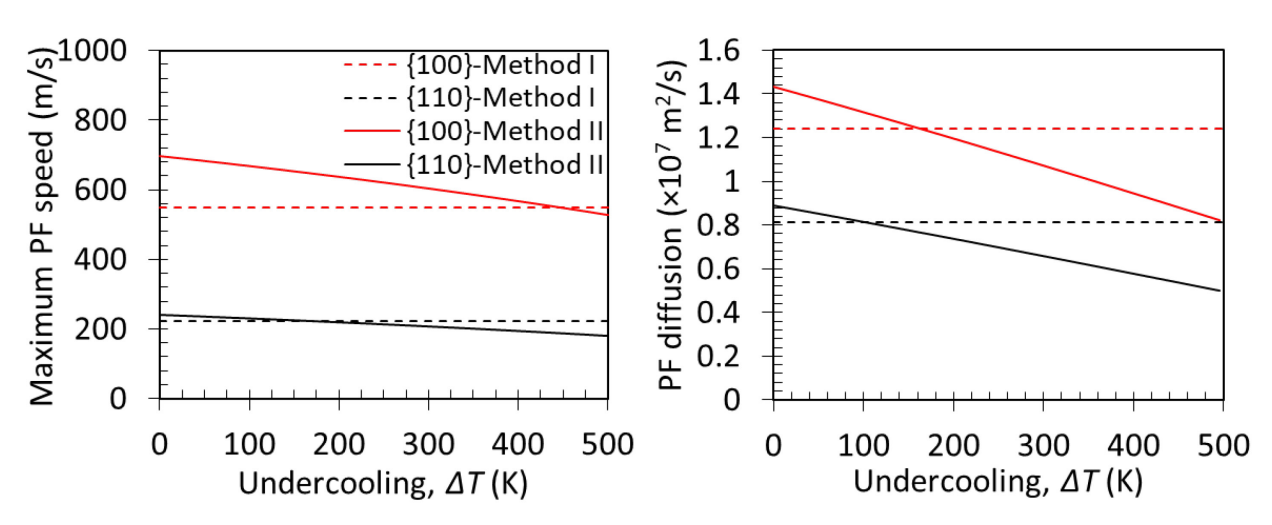


Figure 6. The maximum speed of PF propagation, V_{φ} , and the PF diffusion coefficient, D_{φ} , as a function of undercooling obtained from Methods I and II.

To show that the conclusions of this study are not limited to Ni and are applicable to any fcc materials, we have performed the following analytical analysis. For velocity range $V < V_{\varphi}$, reformatting Eq. (8) suggests that this equation is a function of V and D_{φ} , which are both functions of ΔT :

$$\ell = l_0 \left[1 - \frac{V^2}{\frac{D_{\varphi}}{\tau_{\varphi}}} \right]^{1/2}. \tag{19}$$

Therefore, one gets

$$\frac{d\ell}{d(\Delta T)} = \frac{\partial \ell}{\partial V} \frac{\partial V}{\partial (\Delta T)} + \frac{\partial \ell}{\partial D_{\varphi}} \frac{\partial D_{\varphi}}{\partial (\Delta T)}.$$
 (20)

Multiplying both sides in $d(\Delta T)/dV$ gives:

$$\frac{d\ell}{dV} = \frac{\partial\ell}{\partial V} + \frac{\partial\ell}{\partial D_{\varphi}} \frac{\partial D_{\varphi}}{\partial(\Delta T)} \frac{d(\Delta T)}{dV}.$$
 (21)

Substituting ℓ and D_{φ} from Eqs. (19) and (7) in Eq. (21) is, finally, provides:

$$\frac{d\ell}{dV} = \frac{l_0}{2} \frac{\frac{V}{D_{\varphi}/\tau_{\varphi}}}{\left[1 - \frac{V^2}{\frac{D_{\varphi}}{\tau_{\varphi}}}\right]^{1/2}} \left\{-2 + V\left(-\frac{E_A/k_B}{(T_m - \Delta T)^2}\right) \frac{d(\Delta T)}{dV}\right\} \tag{22}$$

For a fixed velocity, the results in Figure 2 suggest that both ΔT and $\frac{d(\Delta T)}{dV}$ for {110} interface are much larger than those for {100} interface. This conclusion was observed in other MD simulation studies on several fcc elements [35, 69, 71, 85, 86]. Therefore, a_2 term for fcc metals is generally larger for the {110} interface. On the other hand, the results in Figure 6 suggest that the PF diffusion coefficient of {100} interface, over the entire investigated undercooling range, is smaller than that of {110} interface. Therefore, a_1 term for {110} interface is also much larger than {100} interface. In general, the variation of interface width with velocity $(d\ell/dV)$ is much stronger for {110} interface than {100} interface. Our MD results (presented in Figure 5) support this conclusion, and the parameter controlling the rate, V_{φ} , is smaller for {110} interface in comparison to {100} interface.

3.5 Prediction of Interface Velocity versus Undercooling by Kinetic Phase-Field Model

To test the accuracy of atomistic-informed kinetic PF model in simulating rapid solidification, we perform a direct comparison of the interface velocity versus undercooling obtained from MD and PF simulations. Figure 7 summarizes the velocity-undercooling correlation obtained by the atomistic-informed kinetic PF model (methods I and II) and compares them with the results from parabolic PF model and independent MD simulations. The results based on Method I are almost close to the predictions of parabolic PF models (zero τ_{φ}). For small undercooling, there is great compatibility between MD results and those from parabolic and hyperbolic (Method I) PF models. However, as the undercooling increases, the difference between the MD and PF data sets also increases. Despite the slight improvements made by kinetic PF model-Method I, there are still considerable deviations in comparison with the MD results, and this model fails to accurately predict the kinetics of rapid solidification.

During the near-equilibrium solidification (which is analogous to the case with $V_{\varphi} \to \infty$), the SL interface velocity and undercooling hold a linear correlation. However, as phase transformation enter a strongly non-equilibrium range, one should use Eq. (4) to discuss the velocity-undercooling relationship. Eq. (4) suggests that a larger maximum PF propagation speed delays the onset of non-equilibrium solidification to larger driving forces. This occurs because the square-root in Eq. (4) gets closer to 1 for large V_{φ} and, therefore, the linear correlation between velocity and undercooling holds for a wider undercooling range. Based on the values reported in Table 3, one expects the $\{100\}$ -face holds the linearity between interface velocity and undercooling for a larger temperature range. The MD results, as shown in Figure 7, support this conclusion. The velocity obtained from MD simulation of ΔT =200 K still perfectly lies in the linear range for the solidification of $\{100\}$ -face. While for the case of $\{110\}$ -face, the results start deviating from linearity at ΔT ≈180 K. Despite the inaccuracies of the kinetic PF model-Method I, the results are still consistent with our previous statement. Solidification of the $\{100\}$ -face holds its linearity up to 500 K undercooling, while the $\{110\}$ -face results diverge from the linear behavior when undercooling exceeds 350 K.

One should especially note an important feature in the solution of the parabolic model. With

 $\tau_{\varphi} = 0 \ (V_{\varphi} \to \infty)$ the square root in Eq. (4) becomes equal to unity, but the non-equilibrium function D_{ω} given by Eq. (5) still stays in the governing system of algebraic equations. The PF diffusion coefficient D_{ω} is inversely proportional to the viscosity function given by the well-known Vogel-Fulcher-Tammann [87, 88] expression. This viscosity is not a function of an Arrhenius type, but it is derived from a local nonequilibrium theory consistent with the mode-coupling theory [89]. Therefore, the non-equilibrium function D_{φ} cannot remain in the solution of the parabolic model, which is a model based on the hypothesis of local thermodynamic equilibrium. The D_{ω} function in Eq. (7) simply transforms to a constant value in the local equilibrium limit. Taking this constant value from Table 3 and using it in the solution of the parabolic model ($\tau_{\omega} = 0$), one gets a natural result: the interface velocity depends linearly on undercooling, $V \propto \Delta T_k$, see Figure 6. Indeed, as is shown in Figure 7, compatibility of the kinetic PF modeling and the MD-data becomes possible only if the finite relaxation is taken with temperature-dependent material properties based on Method II into account. The comparison shown in Figure 7 states that, first the local nonequilibrium contribution relaxation of the gradient flow, $\partial^2 \varphi / \partial t^2$, in the kinetic PF model is critical for explaining the non-linearity in MD-data for the whole range of investigated undercooling. In addition, it validates the accuracy of the developed MD and PF integration method based on temperature-dependent material properties.

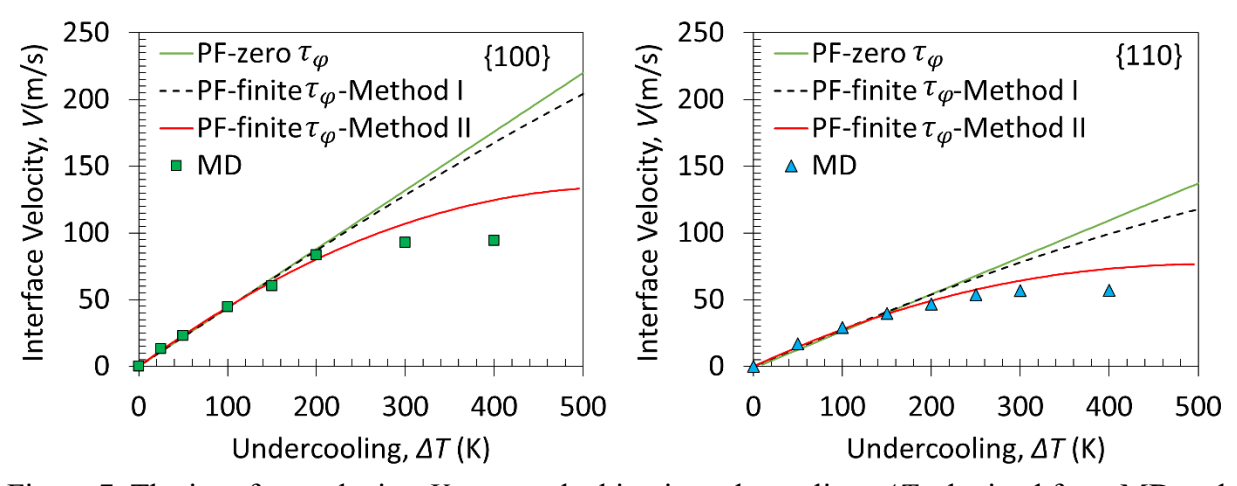


Figure 7. The interface velocity, V, versus the kinetic undercooling, ΔT , obtained from MD and atomistic-informed PF simulations of Ni solidification using the parabolic PF model (zero τ_{φ}) and the hyperbolic (finite τ_{φ}) PF models parametrized based on Methods I and II.

Conclusion

In this study, we proposed integrating a novel MD-based method with the kinetic PF model to obtain a quantitative prediction of rapid solidification in metals. In simulating the rapid solidification, predicting the nonlinearity in velocity-undercooling relationship plays a crucial role. The kinetic PF model considers the local nonequilibrium contribution of the solid-liquid interface and in bulk phases to capture the nonlinearity in rapid solidification kinetics. However, all the

previous studies of the kinetic PF model, instead of predicting the nonlinearity in velocity-undercooling relationship, parameterized the model such that the simulation output fits the target/known nonlinearity. Our goal in this study was to make the kinetic PF model be predictive of this nonlinearity by integrating the model with MD simulation data.

In addition to the SL interface free energy and kinetic coefficient, we need two additional material properties to parameterize the kinetic PF model, namely maximum PF propagation velocity, V_{φ} , and PF diffusion coefficient, D_{φ} . We used the traveling wave solution of the hyperbolic PF equation to propose two new computational approaches for calculating the mean and temperature-dependent V_{φ} and D_{φ} . MD calculations provided two independent datasets describing the dynamic variations of the diffuse interface width and nonlinearity of velocityundercooling relationship. While the former was used to calculate the target material properties and determine the model parameters, the latter was used to validate the predictions of the multiscale modeling. The SL interface width presents a descending behavior as the solidification velocity increases, and the {110} crystallographic face presents a more dramatic change in comparison to {100} face at a given undercooling, with the corresponding mean values of V_{ω} =550±39 and 224±8 m/s, respectively. These values suggest that the onset of non-equilibrium solidification kinetics for the {110} interface takes place at a smaller undercooling, and this observation was also confirmed to be valid for any fcc metals by analytical analysis of the variation of interface width versus interface velocity. The results of free solidification simulations by MD and atomistic-informed kinetic PF model supported this conclusion. The parabolic PF model predicts a linear relationship between interface velocity and undercooling even at high-velocity solidification range. The kinetic PF models using the temperature-independent material properties predicts a slightly non-linear relationship between interface velocity and undercooling. The kinetic PF model parametrized by temperature-dependent material properties leads to a more accurate prediction of the velocity-undercooling nonlinear relationship at higher undercoolings.

CRediT Authorship Contribution Statement

Sepideh Kavousi: Conceptualization, Methodology, Software, Formal analysis, Writing – original draft. **Vladimir Ankudinov:** Methodology, Formal analysis, Writing – review & editing. **Peter K. Galenko:** Conceptualization, Methodology, Formal analysis, Writing – review & editing. **Mohsen Asle Zaeem:** Supervision, Conceptualization, Methodology, Formal analysis, Writing – review & editing, Funding acquisition.

Declaration of Competing Interest

The authors declare that they have no known competing financial interests or personal relationships that could have appeared to influence the work reported in this paper.

Acknowledgment

This study was supported by the National Science Foundation, NSF-CMMI 2031800, and by Russian Science Foundation under 21-19-00279. S. Kavousi and M. Asle Zaeem are grateful for the supercomputing time allocation provided by the NSF's ACCESS (Advanced Cyberinfrastructure Coordination Ecosystem: Services & Support), Award No. TG-DMR140008.

APPENDIX

Table A1: The variations of undercooling ΔT (K), average of interface width l (Å), and average solidification velocity V (m/s) for {100} and {110} crystal faces.

{100} crystal face		{110} crystal face			
$\Delta T(K)$	Average V (m/s)	Average <i>l</i> (Å)	$\Delta T(K)$	Average V (m/s)	Average <i>l</i> (Å)
300	92.95674	22.90817	300	56.86198	22.39815
250	117.6372	22.8	250	53.61786	22.1
200	83.48153	23.03791	200	46.78239	22.21412
150	60.18601	23.15211	150	39.67895	22.3209
100	44.64692	23.17693	100	29.06593	22.43
50	22.92245	23.32794	50	16.90863	22.58
25	13.26536	23.3861	0	0	22.81051
0	0	23.41			

REFERENCES

- [1] S. Ghosh, Predictive modeling of solidification during laser additive manufacturing of nickel superalloys: recent developments, future directions, Materials Research Express, 5 (2018) 012001.
- [2] E. Nuñez-Mendoza, E. López Cuellar, W. Benicio de Castro, B. López Walle, Effect of the linear velocity during the melt spinning process on shape memory transformation of Ni-Ti ribbons, MRS Proceedings, 1373 (2012) imrc-1373-s1374-1319.
- [3] B. Song, X. Zhao, S. Li, C. Han, Q. Wei, S. Wen, J. Liu, Y. Shi, Differences in microstructure and properties between selective laser melting and traditional manufacturing for fabrication of metal parts: A review, Frontiers of Mechanical Engineering, 10 (2015) 111-125.
- [4] V.I. Tkatch, A.I. Limanovskii, S.N. Denisenko, S.G. Rassolov, The effect of the melt-spinning processing parameters on the rate of cooling, Materials Science and Engineering: A, 323 (2002) 91-96.
- [5] O.V. Gusakova, P.K. Galenko, V.G. Shepelevich, D.V. Alexandrov, M. Rettenmayr, Diffusionless (chemically partitionless) crystallization and subsequent decomposition of supersaturated solid solutions in Sn-Bi eutectic alloy, Philosophical Transactions of the Royal Society A: Mathematical, Physical and Engineering Sciences, 377 (2019) 20180204.
- [6] G. Matache, M. Vladut, A. Paraschiv, R.M. Condruz, Edge and corner effects in selective laser melting of IN 625 alloy, Manufacturing Rev., 7 (2020) 8.
- [7] W. Yuan, H. Chen, T. Cheng, Q. Wei, Effects of laser scanning speeds on different states of the molten pool during selective laser melting: Simulation and experiment, Materials & Design, 189 (2020) 108542. [8] I.S. Miroshnichenko, Quenching from the liquid state, Metallurgiya, Moscow, 1982.
- [9] A.A. Chernov, Modern crystallography III: crystal growth, Springer Science & Business Media2012. [10] D.M. Herlach, Metastable solids from undercooled melts, Materials science forum, Trans Tech Publ, 2007, pp. 1977-1982.

- [11] P.K. Galenko, D. Jou, Rapid solidification as non-ergodic phenomenon, Physics Reports, 818 (2019) 1-70.
- [12] C. Lai, H. Wang, Q. Pu, T. Xu, J. Yang, X. Zhang, F. Liu, Phase selection and re-melting-induced anomalous eutectics in undercooled Ni–38 wt% Si alloys, Journal of Materials Science, 51 (2016) 10990-11001.
- [13] H.W. Wilson, XX. On the velocity of solidification and viscosity of super-cooled liquids, The London, Edinburgh, and Dublin Philosophical Magazine and Journal of Science, 50 (1900) 238-250.
- [14] F. MacDougall, Kinetic Theory of Liquids. By J. Frenkel, The Journal of Physical Chemistry, 51 (1947) 1032-1033.
- [15] D. Turnbull, On the relation between crystallization rate and liquid structure, The Journal of Physical Chemistry, 66 (1962) 609-613.
- [16] J.Q. Broughton, G.H. Gilmer, K.A. Jackson, Crystallization Rates of a Lennard-Jones Liquid, Physical Review Letters, 49 (1982) 1496-1500.
- [17] A. Salhoumi, P. Galenko, Analysis of interface kinetics: solutions of the Gibbs Thomson-type equation and of the Kinetic Rate Theory, IOP Conf. Ser.: Mater. Sci. Eng. 2017.
- [18] P.K. Galenko, V. Ankudinov, Local non-equilibrium effect on the growth kinetics of crystals, Acta Materialia, 168 (2019) 203-209.
- [19] V. Borisov, Theory of the Two-Phase Zone of a Metal Ingot, Moscow, Metallurgiya, DOI (1987).
- [20] M.I. Mendelev, M.J. Rahman, J.J. Hoyt, M. Asta, Molecular-dynamics study of solid–liquid interface migration in fcc metals, Modelling and Simulation in Materials Science and Engineering, 18 (2010) 074002.
- [21] Y. Ashkenazy, R.S. Averback, Atomic mechanisms controlling crystallization behaviour in metals at deep undercoolings, Europhysics Letters (EPL), 79 (2007) 26005.
- [22] A. Kerrache, J. Horbach, K. Binder, Molecular-dynamics computer simulation of crystal growth and melting in Al 50 Ni 50, EPL (Europhysics Letters), 81 (2008) 58001.
- [23] Q. Yang, H. Liu, H. Peng, Crystal growth in deeply undercooled Ni₅₀Al₅₀: Signature of the ordering sequence at the interface, J Chem Phys, 154 (2021) 194503.
- [24] W.-L. Chan, R.S. Averback, D.G. Cahill, Y. Ashkenazy, Solidification Velocities in Deeply Undercooled Silver, Physical Review Letters, 102 (2009) 095701.
- [25] J.J. Hoyt, B. Sadigh, M. Asta, S.M. Foiles, Kinetic phase field parameters for the Cu–Ni system derived from atomistic computations, Acta Materialia, 47 (1999) 3181-3187.
- [26] R. Kobayashi, Modeling and numerical simulations of dendritic crystal growth, Physica D: Nonlinear Phenomena, 63 (1993) 410-423.
- [27] R. Kobayashi, A Numerical Approach to Three-Dimensional Dendritic Solidification, Experimental Mathematics, 3 (1994) 59-81.
- [28] W.J. Boettinger, J.A. Warren, The phase-field method: simulation of alloy dendritic solidification during recalescence, Metallurgical and Materials Transactions A, 27 (1996) 657-669.
- [29] G. Caginalp, Phase Field Models and Sharp Interface Limits: Some Differences in Subtle Situations, Rocky Mountain J. Math., 21 (1991) 603-615.
- [30] N. Moelans, B. Blanpain, P. Wollants, An introduction to phase-field modeling of microstructure evolution, Calphad, 32 (2008) 268-294.
- [31] I. Steinbach, Phase-field models in materials science, Modelling and Simulation in Materials Science and Engineering, 17 (2009) 073001.
- [32] S. Wang, M. Asle Zaeem, M.F. Horstemeyer, P.T. Wang, Investigating thermal effects on morphological evolution during crystallisation of hcp metals: three-dimensional phase field study, Materials Technology, 27 (2012) 355-363.
- [33] O. Penrose, P.C. Fife, Thermodynamically consistent models of phase-field type for the kinetic of phase transitions, Physica D: Nonlinear Phenomena, 43 (1990) 44-62.

- [34] S. Kavousi, D. Moldovan, Phase Field Modeling of Solidification in Single Component Systems, ASME 2017 International Mechanical Engineering Congress and Exposition, American Society of Mechanical Engineers, 2017, pp. V014T011A034-V014T011A034.
- [35] G. Azizi, S. Kavousi, M. Asle Zaeem, Interactive effects of interfacial energy anisotropy and solute transport on solidification patterns of Al-Cu alloys, Acta Materialia, 231 (2022) 117859.
- [36] M. Asle Zaeem, H. Yin, S.D. Felicelli, Modeling dendritic solidification of Al–3%Cu using cellular automaton and phase-field methods, Applied Mathematical Modelling, 37 (2013) 3495-3503.
- [37] M. Asle Zaeem, H. Yin, S.D. Felicelli, Comparison of Cellular Automaton and Phase Field Models to Simulate Dendrite Growth in Hexagonal Crystals, Journal of Materials Science & Technology, 28 (2012) 137-146.
- [38] M. Berghoff, M. Selzer, B. Nestler, Phase-Field Simulations at the Atomic Scale in Comparison to Molecular Dynamics, The Scientific World Journal, 2013 (2013) 564272.
- [39] J. Bragard, A. Karma, Y.H. Lee, M. Plapp, Linking phase-field and atomistic simulations to model dendritic solidification in highly undercooled melts, Interface Science, 10 (2002) 121-136.
- [40] S. Kavousi, B.R. Novak, M. Asle Zaeem, D. Moldovan, Combined molecular dynamics and phase field simulation investigations of crystal-melt interfacial properties and dendritic solidification of highly undercooled titanium, Computational Materials Science, 163 (2019) 218-229.
- [41] S. Kavousi, A. Gates, L. Jin, M. Asle Zaeem, A Temperature-Dependent Atomistic-Informed Phase-Field Model to Study Dendritic Growth, Journal of Crystal Growth, 579 (2021) 126461.
- [42] M. Guerdane, M. Berghoff, Crystal-melt interface mobility in bcc Fe: Linking molecular dynamics to phase-field and phase-field crystal modeling, Physical Review B, 97 (2018) 144105.
- [43] C. Tang, P. Harrowell, Anomalously slow crystal growth of the glass-forming alloy CuZr, Nature Materials, 12 (2013) 507-511.
- [44] P.K. Galenko, L.V. Toropova, D.V. Alexandrov, G. Phanikumar, H. Assadi, M. Reinartz, P. Paul, Y. Fang, S. Lippmann, Anomalous kinetics, patterns formation in recalescence, and final microstructure of rapidly solidified Al-rich Al-Ni alloys, Acta Materialia, 241 (2022) 118384.
- [45] P. Galenko, E. Abramova, D. Jou, D. Danilov, V. Lebedev, D. Herlach, Solute trapping in rapid solidification of a binary dilute system: A phase-field study, Physical Review E, 84 (2011) 041143-041141-041117.
- [46] P. Galenko, V. Ankudinov, K. Reuther, M. Rettenmayr, A. Salhoumi, E. Kharanzhevskiy, Thermodynamics of rapid solidification and crystal growth kinetics in glass-forming alloys, Philosophical Transactions of the Royal Society A, 377 (2019) 20180205.
- [47] E. Karim, M. He, A. Salhoumi, L. Zhigilei, P. Galenko, Kinetics of solid-liquid interface motion in molecular dynamics and phase-field models: Crystallization of chromium and silicon, Philosophical Transactions of the Royal Society A: Mathematical, Physical and Engineering Sciences, 379 (2021) 20200320.
- [48] V. Ankudinov, K.R. Elder, P.K. Galenko, Traveling waves of the solidification and melting of cubic crystal lattices, Physical Review E, 102 (2020) 062802.
- [49] P.K. Galenko, R. Wonneberger, S. Koch, V. Ankudinov, E.V. Kharanzhevskiy, M. Rettenmayr, Bell-shaped "dendrite velocity-undercooling" relationship with an abrupt drop of solidification kinetics in glass forming Cu-Zr(-Ni) melts, Journal of Crystal Growth, 532 (2020) 125411.
- [50] A. Salhoumi, P.K. Galenko, Fast traveling waves in the phase-field theory: effective mobility approach versus kinetic energy approach, Journal of Physics: Condensed Matter, 32 (2020) 204003.
- [51] J.J. Hoyt, M. Asta, A. Karma, Method for Computing the Anisotropy of the Solid-Liquid Interfacial Free Energy, Physical Review Letters, 86 (2001) 5530-5533.
- [52] S. Kavousi, B.R. Novak, M.I. Baskes, M. Asle Zaeem, D. Moldovan, Modified embedded-atom method potential for high-temperature crystal-melt properties of Ti–Ni alloys and its application to phase field simulation of solidification, Modelling and Simulation in Materials Science and Engineering,

- 28 (2019) 015006.
- [53] S. Lippmann, C. Simon, S. Zechel, M. Seyring, U.S. Schubert, G. Wilde, M. Rettenmayr, Determining solid/liquid interfacial energies in Al-Cu by curvature controlled melting point depression, Acta Materialia, 147 (2018) 113-121.
- [54] J. Monk, Y. Yang, M.I. Mendelev, M. Asta, J.J. Hoyt, D.Y. Sun, Determination of the crystal-melt interface kinetic coefficient from molecular dynamics simulations, Modelling and Simulation in Materials Science and Engineering, 18 (2010) 015004.
- [55] S. Kavousi, B.R. Novak, J. Hoyt, D. Moldovan, Interface kinetics of rapid solidification of binary alloys by atomistic simulations: Application to Ti-Ni alloys, Computational Materials Science, 184 (2020) 109854.
- [56] Y. Yang, H. Humadi, D. Buta, B.B. Laird, D. Sun, J.J. Hoyt, M. Asta, Atomistic Simulations of Nonequilibrium Crystal-Growth Kinetics from Alloy Melts, Physical Review Letters, 107 (2011) 025505.
- [57] S. Kavousi, B.R. Novak, D. Moldovan, M. Asle Zaeem, Quantitative prediction of rapid solidification by integrated atomistic and phase-field modeling, Acta Materialia, 211 (2021) 116885.
- [58] P. Galenko, D. Jou, Diffuse-interface model for rapid phase transformations in nonequilibrium systems, Physical Review E, 71 (2005) 046125.
- [59] M. Leontovich, L. Mandelshtam, To the theory of the absorption of sound in liquids, Zh. Eksp. Teor. Fiz., [Sov. Phys. JETP], 7 (1937) 438-453.
- [60] V.L. Ginzburg, L.D. Landau, On the theory of superconductivity, On superconductivity and superfluidity, Springer2009, pp. 113-137.
- [61] L.D. Landau, I.M. Khalatnikov, On the anomalous absorption of sound near a second order phase transition point, Dokladii Academii Nauk CCCP, 96 (1954) 469-472.
- [62] B. Echebarria, R. Folch, A. Karma, M. Plapp, Quantitative phase-field model of alloy solidification, Physical Review E, 70 (2004) 061604.
- [63] R.A. Fisher, The wave of advance of advantageous genes, Annals of eugenics, 7 (1937) 355-369.
- [64] A. Kolmogorov, I. Petrovskii, N. Piscounov, A study of the diffusion equation with increase in the amount of substance, and its application to a biological problem. VM Tikhomirov editor, Selected Works of A, DOI (1937).
- [65] S.M. Allen, J.W. Cahn, Mechanisms of phase transformations within the miscibility gap of Fe-rich Fe-Al alloys, Acta Metallurgica, 24 (1976) 425-437.
- [66] S.M. Allen, J.W. Cahn, Coherent and incoherent equilibria in iron-rich iron-aluminum alloys, Acta Metallurgica, 23 (1975) 1017-1026.
- [67] I.G. Nizovtseva, P.K. Galenko, D.V. Alexandrov, The hyperbolic Allen–Cahn equation: exact solutions, Journal of Physics A: Mathematical and Theoretical, 49 (2016) 435201.
- [68] P. Galenko, A. Salhoumi, The hodograph equation for slow and fast anisotropic interface propagation, Philosophical Transactions of the Royal Society A, 379 (2021) 20200324.
- [69] J.J. Hoyt, M. Asta, Atomistic computation of liquid diffusivity, solid-liquid interfacial free energy, and kinetic coefficient in Au and Ag, Physical Review B, 65 (2002) 214106.
- [70] S. Kavousi, B.R. Novak, M.I. Baskes, M. Asle Zaeem, D. Moldovan, Modified embedded-atom method potential for high-temperature crystal-melt properties of Ti–Ni alloys and its application to phase field simulation of solidification, Modelling and Simulation in Materials Science and Engineering, 28 (2020) 015006.
- [71] D.Y. Sun, M. Asta, J.J. Hoyt, Kinetic coefficient of Ni solid-liquid interfaces from molecular-dynamics simulations, Physical Review B, 69 (2004) 024108.
- [72] E. Asadi, M. Asle Zaeem, S. Nouranian, M.I. Baskes, Quantitative modeling of the equilibration of two-phase solid-liquid Fe by atomistic simulations on diffusive time scales, Physical Review B, 91 (2015) 024105.
- [73] E. Asadi, M. Asle Zaeem, S. Nouranian, M.I. Baskes, Two-phase solid-liquid coexistence of Ni, Cu,

- and Al by molecular dynamics simulations using the modified embedded-atom method, Acta Materialia, 86 (2015) 169-181.
- [74] W.R. Fehlner, S.H. Vosko, A product representation for cubic harmonics and special directions for the determination of the Fermi surface and related properties, Canadian Journal of Physics, 54 (1976) 2159-2169.
- [75] S. Plimpton, Fast Parallel Algorithms for Short-Range Molecular Dynamics, Journal of Computational Physics, 117 (1995) 1-19.
- [76] R.T. McGibbon, K.A. Beauchamp, M.P. Harrigan, C. Klein, J.M. Swails, C.X. Hernández, C.R. Schwantes, L.-P. Wang, T.J. Lane, V.S. Pande, MDTraj: A Modern Open Library for the Analysis of Molecular Dynamics Trajectories, Biophys J, 109 (2015) 1528-1532.
- [77] M. Newville, T. Stensitzki, D. B. Allen, A. Ingargiola, LMFIT: Non-Linear Least-Square Minimization and Curve-Fitting for Python¶, 2014.
- [78] A. Stukowski, Visualization and analysis of atomistic simulation data with OVITO—the Open Visualization Tool, Modelling and Simulation in Materials Science and Engineering, 18 (2009) 015012.
- [79] E. Burke, J.Q. Broughton, G.H. Gilmer, Crystallization of fcc (111) and (100) crystal-melt interfaces: A comparison by molecular dynamics for the Lennard-Jones system, The Journal of Chemical Physics, 89 (1988) 1030-1041.
- [80] F. Celestini, J.-M. Debierre, Measuring kinetic coefficients by molecular dynamics simulation of zone melting, Physical Review E, 65 (2002) 041605.
- [81] V. Borovikov, M.I. Mendelev, A.H. King, Effects of stable and unstable stacking fault energy on dislocation nucleation in nano-crystalline metals, Modelling and Simulation in Materials Science and Engineering, 24 (2016) 085017.
- [82] C. Yang, L. Liu, X. Zhao, Y. Li, J. Zhang, H. Fu, Dendrite morphology and evolution mechanism of nickel-based single crystal superalloys grown along the <001> and <011> orientations, Progress in Natural Science: Materials International, 22 (2012) 407-413.
- [83] M. Asta, J. Hoyt, A. Karma, Calculation of alloy solid-liquid interfacial free energies from atomic-scale simulations, Physical Review B, 66 (2002) 100101.
- [84] H. Jones, The solid–liquid interfacial energy of metals: calculations versus measurements, Materials Letters, 53 (2002) 364-366.
- [85] E. Asadi, M. Asle Zaeem, S. Nouranian, M. I. Baskes, Two-Phase Solid—Liquid Coexistence of Ni, Cu, and Al by Molecular Dynamics Simulations Using the Modified Embedded-Atom Method, 2015.
- [86] Y.F. Gao, Y. Yang, D.Y. Sun, M. Asta, J.J. Hoyt, Molecular dynamics simulations of the crystal–melt interface mobility in HCP Mg and BCC Fe, Journal of Crystal Growth, 312 (2010) 3238-3242.
- [87] G. Tammann, W. Hesse, Die Abhängigkeit der Viscosität von der Temperatur bie unterkühlten Flüssigkeiten, Zeitschrift für anorganische und allgemeine Chemie, 156 (1926) 245-257.
- [88] G.S. Fulcher, ANALYSIS OF RECENT MEASUREMENTS OF THE VISCOSITY OF GLASSES, Journal of the American Ceramic Society, 8 (1925) 339-355.
- [89] M.G. Vasin, V.M. Vinokur, Description of glass transition kinetics in 3D XY model in terms of gauge field theory, Physica A: Statistical Mechanics and its Applications, 525 (2019) 1161-1169.